

Successive phase transitions and magnetization plateau in the spin-1 triangular-lattice antiferromagnet $\text{Ba}_2\text{La}_2\text{NiTe}_2\text{O}_{12}$ with small easy-axis anisotropy

Mutsuki Saito^{1,*}, Masari Watanabe¹, Nobuyuki Kurita¹, Akira Matsuo²,

Koichi Kindo², Maxim Avdeev^{3,4}, Harald O. Jeschke⁵, and Hidekazu Tanaka^{1†}

¹*Department of Physics, Tokyo Institute of Technology, Meguro-ku, Tokyo 152-8551, Japan*

²*Institute for Solid State Physics, University of Tokyo, Kashiwa, Chiba 277-8581, Japan*

³*Australian Nuclear Science and Technology Organisation, Lucas Heights, NSW 2234, Australia*

⁴*School of Chemistry, The University of Sydney, Sydney 2006, Australia*

⁵*Research Institute for Interdisciplinary Science, Okayama University, Kita-ku, Okayama 700-8530, Japan*

(Dated: August 28, 2019)

The crystal structure and magnetic properties of the spin-1 triangular-lattice antiferromagnet $\text{Ba}_2\text{La}_2\text{NiTe}_2\text{O}_{12}$ are reported. Its crystal structure is trigonal $R\bar{3}$, which is the same as that of $\text{Ba}_2\text{La}_2\text{NiW}_2\text{O}_{12}$ [Y. Doi *et al.*, *J. Phys.: Condens. Matter* **29**, 365802 (2017)]. However, the exchange interaction $J/k_B \simeq 19$ K is much greater than that observed in the tungsten system. At zero magnetic field, $\text{Ba}_2\text{La}_2\text{NiTe}_2\text{O}_{12}$ undergoes successive magnetic phase transitions at $T_{N1} = 9.8$ K and $T_{N2} = 8.9$ K. The ground state is accompanied by a weak ferromagnetic moment. These results indicate that the ground-state spin structure is a triangular structure in a plane perpendicular to the triangular lattice owing to the small easy-axis-type anisotropy. The magnetization curve exhibits the one-third plateau characteristic of a two-dimensional triangular-lattice Heisenberg-like antiferromagnet. Exchange constants are also evaluated using density functional theory (DFT). The DFT results demonstrate the large difference in the exchange constants between tellurium and tungsten systems and the good two-dimensionality of the tellurium system.

PACS numbers: 75.10.Jm, 75.45.+j, 61.05.F-, 75.30.Et

I. INTRODUCTION

Triangular-lattice antiferromagnets (TLAFs) exhibit a variety of phase transitions in magnetic fields depending on magnetic anisotropy, spatial anisotropy and interlayer exchange interaction [1, 2]. In particular, the magnetization plateau in TLAF has been attracting considerable attention. For two-dimensional (2D) classical spin TLAF with the easy-axis anisotropy, a magnetization plateau emerges at one-third of the saturation magnetization when a magnetic field is applied parallel to the easy axis [3]. The classical 1/3-magnetization plateau has been observed in quasi-2D large spin TLAFs GdPd_2Al_3 [4, 5] and $\text{Rb}_4\text{Mn}(\text{MoO}_4)_3$ [6].

The easy-axis anisotropy is crucial for stabilizing the 1/3-magnetization plateau in the classical spin TLAF. The plateau is absent in the Heisenberg TLAF and Heisenberg-like TLAF with the easy-plane anisotropy. However, for 2D quantum spin Heisenberg TLAFs, the 1/3-magnetization plateau can be stabilized in a wide magnetic field range by quantum fluctuation [2, 7–18]. The 1/3-magnetization plateau is affected by the magnetic anisotropy. When a magnetic field is applied parallel to the symmetry axis, the magnetic field range of the 1/3-magnetization plateau is enhanced by the easy-axis anisotropy and suppressed by the easy-plane anisotropy [16, 17]. The quantum 1/3-magnetization

plateau has actually been observed in quasi-2D spatially anisotropic TLAF Cs_2CuBr_4 [19–21] and uniform TLAF $\text{Ba}_3\text{CoSb}_2\text{O}_9$ [22–26], both of which have weak antiferromagnetic interlayer exchange interactions, and 3D TLAF CsCuCl_3 [27] with strong ferromagnetic interlayer exchange interaction. All of these compounds have the weak easy-plane anisotropy.

Although the ground states in magnetic fields for the 2D spin-1/2 Heisenberg TLAF are well understood, the effects of the magnetic anisotropy [16, 17], spatial anisotropy [20, 21, 28], interlayer exchange interaction [24, 26, 29], spin quantum number [14, 18] and thermal fluctuation on the ground states and phase diagram have not been sufficiently elucidated.

Recently, magnetic excitations in the spin-1/2 Heisenberg-like TLAF $\text{Ba}_3\text{CoSb}_2\text{O}_9$ were investigated by inelastic neutron scattering experiments [23, 30–32]. Unusual dynamical properties of single-magnon excitations predicted by theory such as the large downward quantum renormalization of excitation energies [33–38] and a rotonlike minimum at the M point [34, 38, 39] were confirmed. A notable feature of the magnetic excitations observed in $\text{Ba}_3\text{CoSb}_2\text{O}_9$ is a three-stage energy structure including intense dispersive excitation continua extending to a high energy six times the exchange constant [31], which cannot be described by the current theory. These experimental results strongly indicate fractionalized spin excitations because the intense excitation continua cannot be explained in terms of conventional two-magnon excitations [39]. For the experimental elucidation of unconventional magnetic excitations, quantum TLAFs with different spin quantum numbers such as spin-1 are nec-

*Electronic address: saito@lee.phys.titech.ac.jp

†Electronic address: tanaka@lee.phys.titech.ac.jp

essary.

In this work, we investigated the crystal structure and magnetic properties of $\text{Ba}_2\text{La}_2\text{NiTe}_2\text{O}_{12}$. Although there is a brief report on the lattice constants and the space group of $\text{Ba}_2\text{La}_2\text{NiTe}_2\text{O}_{12}$ [40], details of the crystal structure and magnetic properties have not been reported. The structure of this compound was found to be the same as that of $\text{Ba}_2\text{La}_2\text{MW}_2\text{O}_{12}$ ($M = \text{Mn, Co, Ni, Zn}$) [41–44], which have a uniform triangular lattice composed of transition metal ions M^{2+} . Figure 1 shows the crystal structure of $\text{Ba}_2\text{La}_2\text{NiTe}_2\text{O}_{12}$. An important feature of the crystal structure is that the magnetic triangular lattices are largely separated by layers of nonmagnetic ions; thus, we can expect good two-dimensionality.

Recently, the magnetic properties in the family of triangular-lattice magnets $\text{Ba}_2\text{La}_2\text{MW}_2\text{O}_{12}$ ($M = \text{Mn, Co, Ni}$) [43, 44] have been investigated by magnetic susceptibility, specific heat and neutron diffraction (ND) measurements. Unfortunately, the exchange interactions were found to be weakly antiferromagnetic [43] or weakly ferromagnetic [44]. It is natural to assume that superexchange interactions between neighboring spins in the same triangular layer occur through $M^{2+} - \text{O}^{2-} - \text{O}^{2-} - M^{2+}$ and $M^{2+} - \text{O}^{2-} - \text{W}^{6+} - \text{O}^{2-} - M^{2+}$ paths. The superexchange through the former path should be antiferromagnetic, while the latter path leads to a ferromagnetic superexchange interaction because the filled outermost orbitals of nonmagnetic W^{6+} and Nb^{5+} ions are $4p$ orbitals, as discussed in Refs. [45, 46]. It is considered that the superexchange interactions via these two paths almost cancel in the tungsten compounds, resulting in a weakly antiferromagnetic or ferromagnetic total exchange interaction. Meanwhile, when the nonmagnetic W^{6+} ion is replaced by a Te^{6+} ion, for which the filled outermost orbital is a $4d$ orbital, the superexchange interaction through the $M^{2+} - \text{O}^{2-} - \text{Te}^{6+} - \text{O}^{2-} - M^{2+}$ path becomes antiferromagnetic and the total exchange interaction should be strongly antiferromagnetic [45, 46].

This is our motivation for studying $\text{Ba}_2\text{La}_2\text{NiTe}_2\text{O}_{12}$. The exchange interaction in the triangular layer was found to be antiferromagnetic and strong as expected. We evaluated individual exchange constants using density functional theory (DFT). The DFT results demonstrate that the nearest-neighbor exchange interaction in the triangular layer is antiferromagnetic and predominant. As shown below, the $1/3$ -magnetization plateau characteristic of the quasi-2D TLAFs was observed in $\text{Ba}_2\text{La}_2\text{NiTe}_2\text{O}_{12}$. This compound is magnetically described as a quasi-2D spin-1 Heisenberg-like TLAF with small easy-axis-type anisotropy.

II. EXPERIMENTAL DETAILS

A powdered sample of $\text{Ba}_2\text{La}_2\text{NiTe}_2\text{O}_{12}$ was prepared by a solid-state reaction in accordance with the chemical reaction $2\text{BaCO}_3 + \text{La}_2\text{O}_3 + \text{NiO} + 2\text{TeO}_2 +$

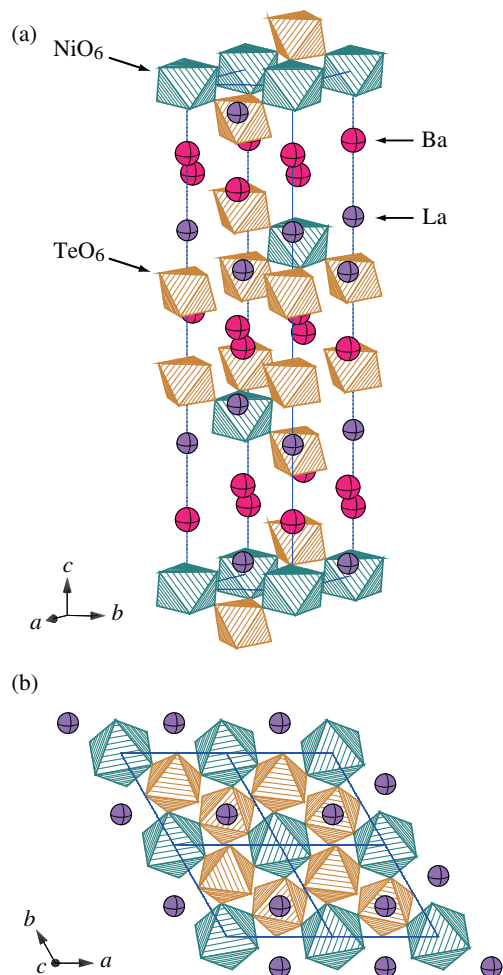


FIG. 1: (Color online) (a) Schematic view of the crystal structure of $\text{Ba}_2\text{La}_2\text{NiTe}_2\text{O}_{12}$. The blue-green and orange octahedra are NiO_6 and TeO_6 octahedra with Ni^{2+} and Te^{6+} ions in the center, respectively. Solid lines denote the chemical unit cell. (b) Crystal structure viewed along the c axis. Magnetic Ni^{2+} ions form a uniform triangular lattice in the ab plane.

$\text{O}_2 \longrightarrow \text{Ba}_2\text{La}_2\text{NiTe}_2\text{O}_{12} + 2\text{CO}_2$ in air. BaCO_3 (Wako, 99.9%), La_2O_3 (Wako, 99.99%), NiO (Wako, 99%) and TeO_2 (Aldrich, 99.995%) were mixed in stoichiometric quantities and calcined at 1000°C in air for one day. $\text{Ba}_2\text{La}_2\text{NiTe}_2\text{O}_{12}$ was sintered at 1000°C for one day after being pressed into a pellet. This sintering process was performed twice. Finally, yellow samples were obtained.

Powder X-ray diffraction (XRD) measurement of $\text{Ba}_2\text{La}_2\text{NiTe}_2\text{O}_{12}$ was conducted using a MiniFlex II diffractometer (Rigaku) with $\text{Cu } K\alpha$ radiation at room temperature. Powder ND measurement was also performed to determine both the crystal and magnetic structures using the high-resolution powder diffractometer Echidna installed at the OPAL reactor of the Australian Nuclear Science and Technology Organisation. The diffraction data were collected with a neutron wavelength of 2.4395 \AA in the temperature range of $1.6 \leq T \leq 14 \text{ K}$.

The crystal structure of $\text{Ba}_2\text{La}_2\text{NiTe}_2\text{O}_{12}$ was refined by Rietveld analysis of the powder XRD and ND data using the RIETAN-FP program [47].

Magnetic measurements in the temperature range of $1.8 \leq T \leq 300$ K and the magnetic field range of $0.1 \leq \mu_0 H \leq 7.0$ T were performed using a Magnetic Property Measurement System (MPMS-XL, Quantum Design). High-field magnetization was measured in a magnetic field of up to $\mu_0 H = 60$ T at $T = 1.3$ K using an induction method with a multilayer pulse magnet at the Institute for Solid State Physics (ISSP), The University of Tokyo. Specific heat measurements in the temperature range of $1.9 \leq T \leq 300$ K at magnetic fields of $\mu_0 H = 0$ and 9 T were performed using a Physical Property Measurement System (PPMS, Quantum Design) by the relaxation method.

III. COMPUTATIONAL DETAILS

We determine the electronic structure of $\text{Ba}_2\text{La}_2\text{NiTe}_2\text{O}_{12}$ by performing all-electron DFT calculations based on the full potential local orbital (FPLO) code [48]. We use the generalized gradient approximation (GGA) exchange and correlation functional [49]. The magnetic exchange interactions are determined by an energy-mapping method [50–52]. We account for the strong electronic correlations on the Ni $3d$ orbitals using the GGA+U exchange correlation functional [53] with the Hund's rule coupling strength $J_H = 0.88$ eV fixed in accordance with the literature [54]. The on-site interaction U is determined using the experimental Curie–Weiss temperature as explained below. As the primitive rhombohedral unit cell of $\text{Ba}_2\text{La}_2\text{NiTe}_2\text{O}_{12}$ in the $R\bar{3}$ space group contains only a single Ni^{2+} ion, we create supercells to allow spin configurations with different energies. A supercell containing four Ni^{2+} ions provides four distinct energies and allows the resolution of nearest- and next-nearest-neighbor coupling in the triangular lattice. A supercell with six Ni^{2+} ions and eight distinct energies is also required to resolve the shortest interlayer exchange path. As is common for triangular lattice antiferromagnets [55], the supercell calculations are computationally demanding, with each formula unit containing one magnetic ion adding more than 100 electrons to the calculation.

IV. RESULTS AND DISCUSSION

A. Crystal structure

The results of the XRD measurement of $\text{Ba}_2\text{La}_2\text{NiTe}_2\text{O}_{12}$ at room temperature and the Rietveld analysis with RIETAN-FP [47] are shown in Fig. 2. First, we chose the structure parameters of $\text{Ba}_2\text{La}_2\text{NiW}_2\text{O}_{12}$ [43, 44] as the initial parameters of the Rietveld analysis, setting the occupancy to 1 for

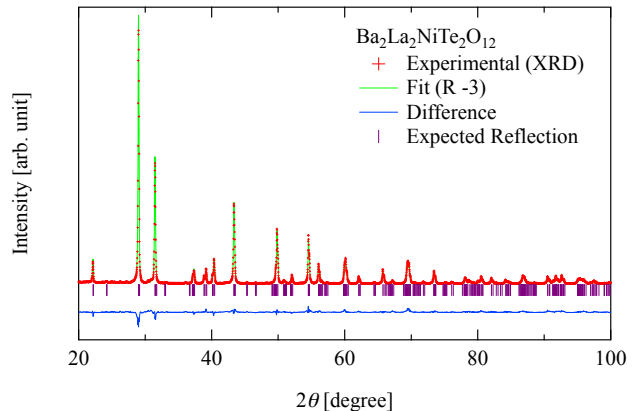


FIG. 2: (Color online) XRD pattern of $\text{Ba}_2\text{La}_2\text{NiTe}_2\text{O}_{12}$ measured at room temperature. Experimental data, the results of Rietveld fitting, their difference and expected reflections are shown by the red symbols, green line, blue line and vertical purple bars, respectively.

TABLE I: Structure parameters of $\text{Ba}_2\text{La}_2\text{NiTe}_2\text{O}_{12}$ determined from the XRD measurement at room temperature.

Atom	Site	x	y	z
Ba	6c	0	0	0.13587(7)
La	6c	0	0	0.28973(6)
Ni	3a	0	0	0
Te	6c	0	0	0.41560(7)
O(1)	18f	0.543(5)	0.514(5)	0.1186(3)
O(2)	18f	0.450(5)	0.473(5)	0.2965(4)
Space group $R\bar{3}$				
$a = 5.681(9)$ Å, $c = 27.60(3)$ Å;				
$R_{\text{wp}} = 12.2\%$, $R_{\text{p}} = 9.4\%$, $R_{\text{e}} = 6.7\%$.				
$B = 1.401$ Å ² for all atoms.				

all atoms and the thermal vibration parameter B to 1.401 Å², which was reported for $\text{Ba}_2\text{La}_2\text{NiW}_2\text{O}_{12}$ [43]. The analysis was based on two structural models with space groups $R\bar{3}m$ and $R\bar{3}$. It is difficult to determine the space group from only the XRD pattern because both structural models successfully reproduce the observed XRD pattern. However, the neutron diffraction pattern obtained at low temperatures above the first ordering temperature $T_{\text{N1}} \simeq 10$ K is much better described by space group $R\bar{3}$ as shown below. The structure parameters refined for space group $R\bar{3}$ using the XRD data are summarized in Table I.

Figure 3 shows the ND pattern of $\text{Ba}_2\text{La}_2\text{NiTe}_2\text{O}_{12}$ measured at low temperatures above the first ordering temperature $T_{\text{N1}} = 9.8$ K, where the diffraction intensity is the average of those measured at $T = 14, 12$ and 10 K. We analyzed the ND data on the basis of two structural models with space groups $R\bar{3}m$ and $R\bar{3}$. The values of R_{wp} and R_{p} are obtained from the refinements to be 22.1% and 15.3% for $R\bar{3}m$ and 7.9% and 5.7% for $R\bar{3}$, re-

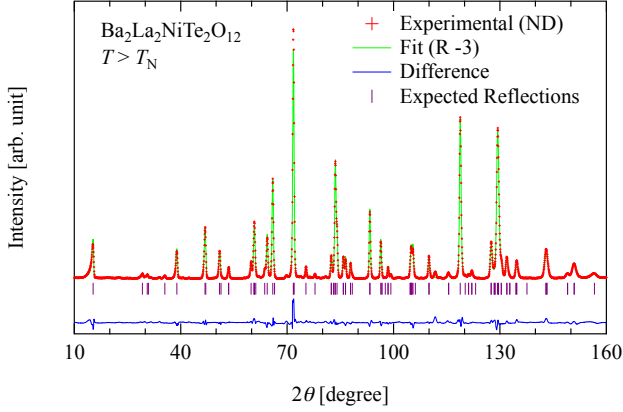


FIG. 3: (Color online) ND pattern of $\text{Ba}_2\text{La}_2\text{NiTe}_2\text{O}_{12}$ measured at low temperatures above the first ordering temperature $T_{N1} = 9.8$ K. Experimental data, the results of Rietveld fitting, their difference and expected reflections are shown by the red symbols, green line, blue line and vertical purple bars, respectively. The experimental data is the average of measurements at $T = 14, 12$ and 10 K.

TABLE II: Structure parameters of $\text{Ba}_2\text{La}_2\text{NiTe}_2\text{O}_{12}$ determined from the ND measurements at several temperatures above $T_{N1} \simeq 10$ K.

Atom	Site	x	y	z	$B [\text{\AA}^2]$
Ba	6c	0	0	0.1370(2)	0.354
La	6c	0	0	0.2890(1)	0.354
Ni	3a	0	0	0	0.437
Te	6c	0	0	0.4150(1)	0.377
O(1)	18f	0.4631(4)	0.4675(5)	0.1168(1)	0.877
O(2)	18f	0.4339(4)	0.4603(5)	0.2947(1)	0.877
Space group $R\bar{3}$					
$a = 5.6682(7)$ \AA , $c = 27.472(2)$ \AA ;					
$R_{\text{wp}} = 7.9\%$, $R_p = 5.7\%$, $R_e = 1.5\%$.					

spectively. The R -factors for $R\bar{3}$ are significantly smaller than those for $R\bar{3}m$. Because no structural phase transition was detected via magnetic susceptibility and specific heat measurements down to 1.8 K, we can conclude that the space group of $\text{Ba}_2\text{La}_2\text{NiTe}_2\text{O}_{12}$ is $R\bar{3}$, which is the same as the space group of $\text{Ba}_2\text{La}_2\text{MW}_2\text{O}_{12}$ ($M = \text{Mn, Co, Ni, Zn}$) [44]. The difference between the crystal structures for these space groups is in the atomic positions of oxygen atoms. Because the atomic scattering factor of oxygen atoms for X-rays is much smaller than those of other atoms, it is difficult to determine the atomic positions of oxygen accurately by XRD measurement, as pointed out by Doi *et al.* [44]. For $R\bar{3}$, NiO_6 and TeO_6 octahedra are rotated in opposite directions around the c axis, which leads to the absence of mirror symmetry, as shown in Fig. 1(b). The structure parameters refined for space group $R\bar{3}$ using the ND data are summarized in Table II.

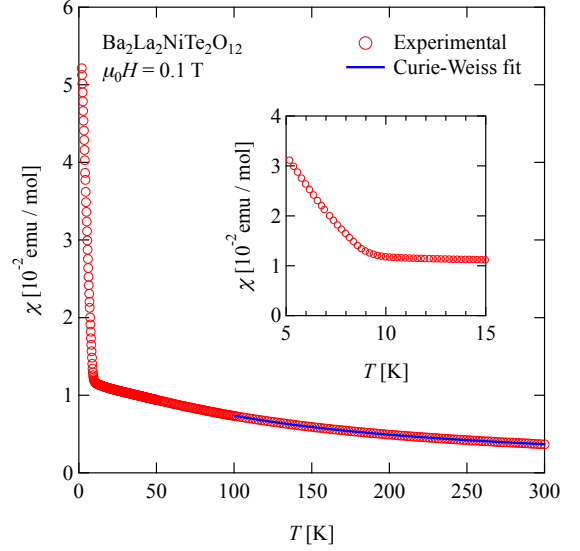


FIG. 4: (Color online) Temperature dependence of the magnetic susceptibility of $\text{Ba}_2\text{La}_2\text{NiTe}_2\text{O}_{12}$ powder measured in an external magnetic field of $\mu_0 H = 0.1$ T. The blue solid line shows the result of a Curie–Weiss fit in the temperature range of $100 \leq T \leq 300$ K. The inset is an enlarged view around 10 K.

B. Magnetic susceptibility and low-field magnetization

The temperature dependence of the magnetic susceptibility of $\text{Ba}_2\text{La}_2\text{NiTe}_2\text{O}_{12}$ powder measured in a magnetic field of $\mu_0 H = 0.1$ T is shown in Fig. 4. The Curie constant $C = 1.482(2)$ emu K mol $^{-1}$ and the Weiss temperature $\Theta_{\text{CW}} = -100.7(3)$ K were obtained by fitting to the Curie–Weiss law $\chi(T) = C/(T - \Theta_{\text{CW}})$ in the temperature range $100 \leq T \leq 300$ K. This large negative Θ_{CW} indicates that the dominant exchange interaction of $\text{Ba}_2\text{La}_2\text{NiTe}_2\text{O}_{12}$ is antiferromagnetic and large, as expected from the superexchange path via the filled outermost $4d$ orbital of Te^{6+} . The exchange constant J , effective magnetic moment μ_{eff} and g -factor are estimated as $J/k_B = 25$ K, $\mu_{\text{eff}} = 3.44 \mu_B$ and $g = 2.4$ on the basis of molecular field theory.

The magnetic susceptibility of $\text{Ba}_2\text{La}_2\text{NiTe}_2\text{O}_{12}$ increases rapidly near 9 K as the temperature decreases, which is indicative of the antiferromagnetic phase transition. This transition temperature of $T_N \simeq 9$ K is lower than $T_N \simeq 13$ K for $\text{Ba}_3\text{NiSb}_2\text{O}_9$ [56, 57], which is an $S = 1$ TLAF with a crystal structure and exchange interaction $J/k_B \simeq 20$ K, similar to those of $\text{Ba}_2\text{La}_2\text{NiTe}_2\text{O}_{12}$ [14, 56, 57]. Thus, the two-dimensionality in $\text{Ba}_2\text{La}_2\text{NiTe}_2\text{O}_{12}$ is better than that in $\text{Ba}_3\text{NiSb}_2\text{O}_9$. Note that the magnetic susceptibility of $\text{Ba}_3\text{NiSb}_2\text{O}_9$ powder does not show a rapid upturn below T_N [56].

A notable feature of the magnetic susceptibility in $\text{Ba}_2\text{La}_2\text{NiTe}_2\text{O}_{12}$ is the rapid increase below T_N . This

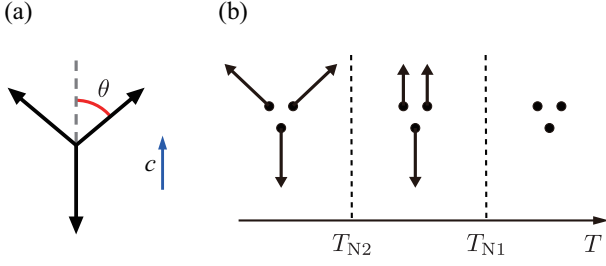


FIG. 5: (Color online) (a) Triangular structure in a plane including the c axis for TLAF with small easy-axis-type anisotropy. The angle θ between canted sublattice spins and the c axis is smaller than 60° . (b) Schematic view of the successive magnetic phase transitions in the TLAF with small easy-axis-type anisotropy and the spin structures in each phase.

behavior can be understood in terms of a small easy-axis-type anisotropy and a ferromagnetic interlayer exchange interaction. When the magnetic anisotropy is of the easy-axis type and small, the spin configuration in the ground state is a triangular structure in a plane including the crystallographic c axis, as shown in Fig. 5(a). The triangular structure is slightly distorted from a perfect 120° structure. The angle θ between canted sublattice spins and the c axis is smaller than 60° . Therefore, the sum of the magnetic moments of three sublattice spins is nonzero; thus, a resultant magnetic moment along the c axis appears in a triangular layer. When the interlayer exchange interaction is antiferromagnetic, the resultant magnetic moments appearing in the neighboring triangular layers are canceled out. On the other hand, when the interlayer exchange interaction is ferromagnetic, all the resultant magnetic moments appearing in the triangular layers align in the same direction, giving the system a net magnetic moment along the c axis. The small easy-axis-type anisotropy of $\text{Ba}_2\text{La}_2\text{NiTe}_2\text{O}_{12}$ is also consistent with the successive magnetic phase transitions observed by the specific heat measurements shown later.

The magnetic field dependence of the magnetization of $\text{Ba}_2\text{La}_2\text{NiTe}_2\text{O}_{12}$ powder is shown in Fig. 6. It is clearly observed that there is a finite magnetization even in zero field. The magnetic moment per spin ΔM in the ground state at zero magnetic field is given by

$$\Delta M = \frac{1}{3}(2 \cos \theta - 1)g\mu_B S, \quad (1)$$

where $S = 1$ and θ is the canting angle shown in Fig. 5(a). The powder average of the weak moment $\overline{\Delta M}$ is given by $\overline{\Delta M} = \Delta M/2$. By using the value $\overline{\Delta M} = 0.015 \mu_B/\text{Ni}^{2+}$, which is obtained by extrapolating the magnetization curve to zero magnetic field, and $g = 2.4$ estimated from the Curie constant, we obtain the angle $\theta = 58.75^\circ$.

The origin of the small easy-axis-type anisotropy is considered to be the single-ion anisotropy expressed as

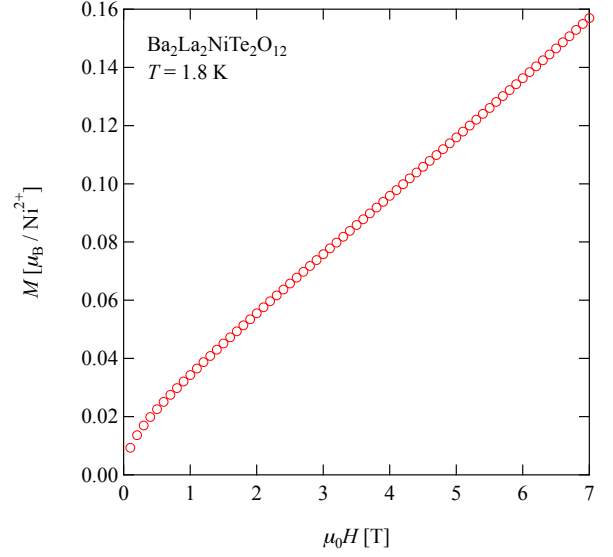


FIG. 6: (Color online) Magnetization curve of $\text{Ba}_2\text{La}_2\text{NiTe}_2\text{O}_{12}$ powder measured at $T = 1.8 \text{ K}$ in magnetic fields up to $\mu_0 H = 7 \text{ T}$.

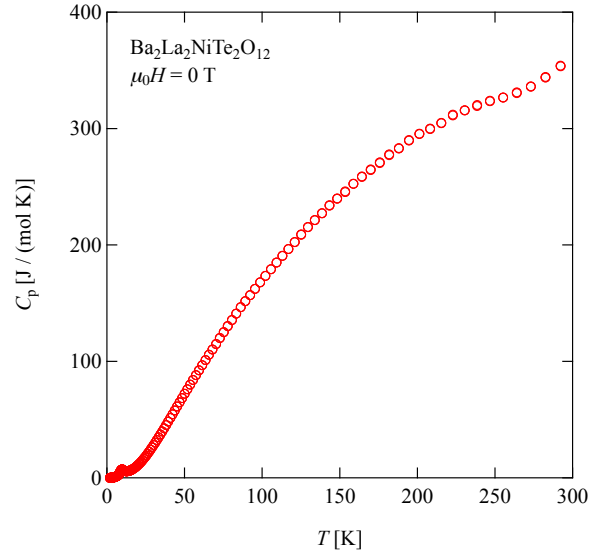


FIG. 7: (Color online) Temperature dependence of the total specific heat of $\text{Ba}_2\text{La}_2\text{NiTe}_2\text{O}_{12}$ powder below 300 K measured at zero magnetic field.

$D(S_i^z)^2$ with $D < 0$. The canting angle θ is expressed as

$$\cos \theta = \frac{3J}{6J - 2|D|}. \quad (2)$$

Using $\theta = 58.75^\circ$, we obtain $|D|/J = 0.108$.

C. Specific heat

The temperature dependence of the specific heat of $\text{Ba}_2\text{La}_2\text{NiTe}_2\text{O}_{12}$ powder below 300 K measured at zero

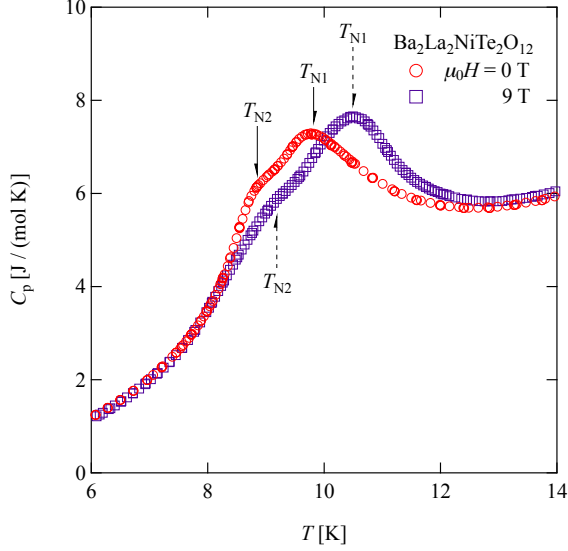


FIG. 8: (Color online) Low-temperature specific heat of $\text{Ba}_2\text{La}_2\text{NiTe}_2\text{O}_{12}$ powder measured at $\mu_0 H = 0$ and 9 T. Arrows indicate magnetic phase transition temperatures T_{N1} and T_{N2} .

magnetic field is shown in Fig. 7. There is no anomaly indicative of a structural phase transition below 300 K. The hump anomaly around room temperature is an extrinsic anomaly that originates from the instability of the temperature. The low-temperature specific heat measured at $\mu_0 H = 0$ and 9 T is shown in Fig. 8. Double peaks indicative of successive magnetic phase transitions are observed at $T_{N1} = 9.8$ K, $T_{N2} = 8.9$ K for $\mu_0 H = 0$ T and at $T_{N1} = 10.5$ K, $T_{N2} = 9.2$ K for $\mu_0 H = 9$ T. Each transition temperature shifts to the high-temperature side with increasing magnetic field, and the shift for T_{N1} is larger than that for T_{N2} .

It is theoretically known that successive magnetic phase transitions occur in a TLAF with easy-axis-type anisotropy [3, 58]. With decreasing temperature, the z components of spins order first at $T = T_{N1}$, and the xy components of spins order next at $T = T_{N2}$, as shown in Fig. 5(b). Similar successive magnetic phase transitions arising from the small easy-axis-type anisotropy were reported for $\text{Ba}_3\text{NiSb}_2\text{O}_9$ [57], which has an exchange constant similar to that of $\text{Ba}_2\text{La}_2\text{NiTe}_2\text{O}_{12}$ [14, 57]. The phase transition temperatures of $\text{Ba}_3\text{NiSb}_2\text{O}_9$ are $T_{N1} = 13.5$ K and $T_{N2} = 13.0$ K, both of which are higher than those of $\text{Ba}_2\text{La}_2\text{NiTe}_2\text{O}_{12}$. This suggests that the two-dimensionality in $\text{Ba}_2\text{La}_2\text{NiTe}_2\text{O}_{12}$ is better than that in $\text{Ba}_3\text{NiSb}_2\text{O}_9$.

Using molecular field theory [58], two transition temperatures are calculated as $T_{N1} = 38.7$ K and $T_{N2} = 37.6$ K with $|D|/J = 0.108$ and the saturation field $H_s = 110$ T obtained below. Although their absolute values are four times larger than those observed, their separation of $T_{N1} - T_{N2} = 1.1$ K is consistent with the experimental separation of 0.9 K.

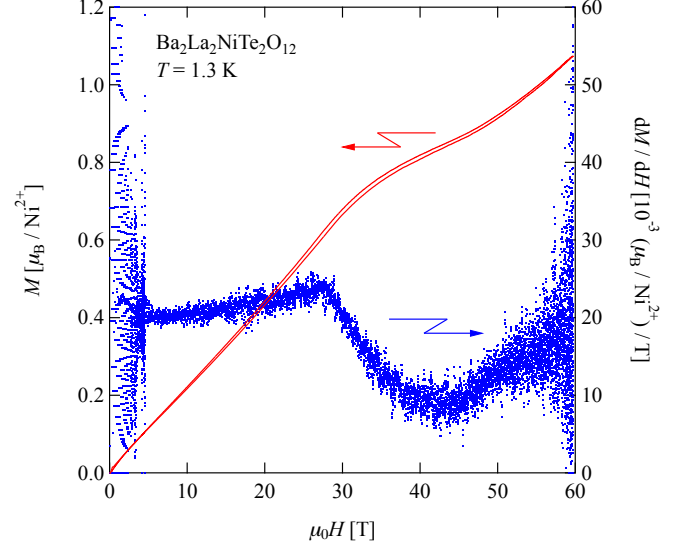


FIG. 9: (Color online) High-field magnetization process of $\text{Ba}_2\text{La}_2\text{NiTe}_2\text{O}_{12}$ measured at 1.3 K upon sweeping the magnetic field up and down. Red solid lines and blue points are the magnetization M and its field derivative dM/dH , respectively.

D. High-field magnetization

The result of the high-field magnetization measurement of $\text{Ba}_2\text{La}_2\text{NiTe}_2\text{O}_{12}$ powder up to 60 T is shown in Fig. 9. The absolute value of the magnetization is calibrated by using the result of the magnetization measurement up to 7 T with a SQUID magnetometer. A magnetization plateau is clearly observed at $M \simeq 0.8 \mu_B / \text{Ni}^{2+}$ for $32 < \mu_0 H < 47$ T. The lower and higher edge fields of the plateau were assigned to the magnetic fields at which dM/dH has inflection points. Because the g -factor estimated from the magnetic susceptibility is $g = 2.4$, the plateau corresponds to the 1/3-magnetization plateau characteristic of the quasi-2D TLAF. The edge fields of the plateau are rather smeared and the plateau is not completely flat. It is expected that this arises from the distribution of the edge fields in the powdered sample owing to the anisotropy of the g -factors and the magnetic anisotropy and not from exchange randomness [59, 60]. When the anisotropy of the g -factor is Δg , the edge fields $H_{c\alpha}$ with $\alpha = 1$ and 2 are distributed in the range of $(\Delta g / \bar{g}) H_{c\alpha}$, where \bar{g} is the average of the g -factor. When the magnetic anisotropy is of the easy-axis type, the field range of the 1/3-plateau becomes wider for $H \parallel c$ and narrower for $H \perp c$ when compared to the Heisenberg model.

Although the classical Heisenberg-like TLAF with easy-axis anisotropy exhibits the 1/3-magnetization plateau, it is difficult to explain the observed magnetization process in terms of a classical spin model only [3]. The lower and higher edge fields of the classical plateau are calculated as $\mu_0 H_{c1} = 34.9$ T and $\mu_0 H_{c2} = 44.6$ T with

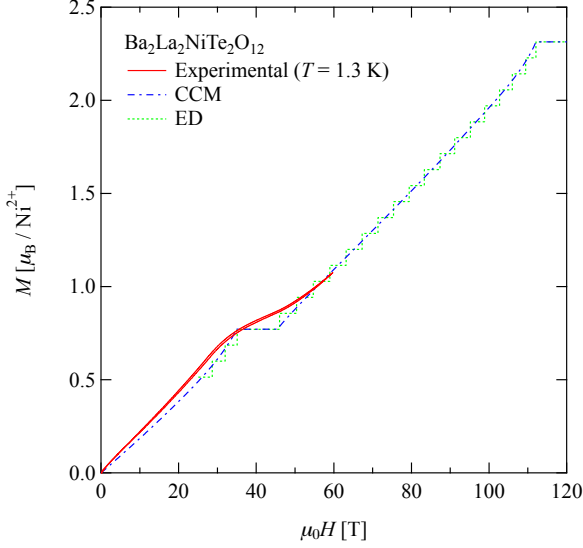


FIG. 10: (Color online) Experimental magnetization curve of $\text{Ba}_2\text{La}_2\text{NiTe}_2\text{O}_{12}$ powder up to 60 T (red line) and theoretical magnetization curves of the $S=1$ Heisenberg TLAF calculated by CCM (blue line) and ED (green line) [14].

$|D|/J=0.108$ and the saturation field $\mu_0 H_s = 110$ T obtained below. The width of the classical plateau is estimated as $\mu_0(H_{c2} - H_{c1}) = 9.7$ T, which is 65 % of observed width of 15 T. It is known that at finite temperature, thermal fluctuation stabilizes the UUD spin state even in the classical spin model, so that the field range of the UUD state increases with increasing temperature [61, 62]. However, in the present case, the effect of the thermal fluctuation should be negligible because the temperature of the magnetization measurement $T = 1.3$ K is much lower than $T_{N2} = 8.9$ K.

For a spin-1 Heisenberg TLAF, the $1/3$ -magnetization plateau is stabilized in a fairly wide magnetic field range by quantum fluctuations [14, 18]. We fit the theoretical magnetization curves of the spin-1 Heisenberg TLAF calculated by the coupled cluster method (CCM) and the exact diagonalization (ED) [14] to our experimental result, as shown in Fig. 10. From this fit, we obtain $\mu_0 H_{c1} = 35$ T, $\mu_0 H_{c2} = 46$ T, $\mu_0 H_s = 110$ T and the saturation magnetization $M_s/\mu_B = 2.31(2)$, which leads to $g = 2.31(2)$. The saturation magnetic field H_s of the spin-1 Heisenberg TLAF is given by $g\mu_B H_s = 9JS$. Using $g \simeq 2.3$ and $H_s \simeq 110$ T, which are estimated from the theoretical magnetization curve fitted to the magnetization data, the exchange interaction is estimated as $J/k_B \simeq 19$ K. This J value is somewhat smaller than $J/k_B = 25$ K estimated from the Weiss constant $\Theta_{CW} = -100.7$ K of the high-temperature magnetic susceptibility. Because the saturation field given by $g\mu_B H_s = 9JS$ is exact, the exchange constant $J/k_B \simeq 19$ K estimated from the saturation field is considered to be more precise.

The magnetic field range of the experimental $1/3$ -plateau $32 < \mu_0 H < 47$ T is somewhat larger than the

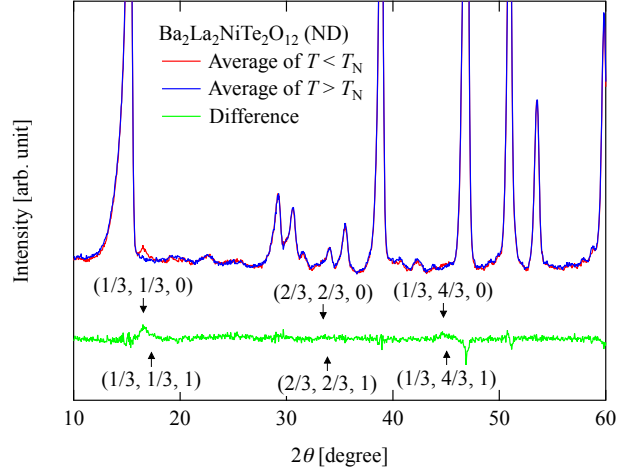


FIG. 11: (Color online) ND intensities of $\text{Ba}_2\text{La}_2\text{NiTe}_2\text{O}_{12}$ powder averaged over $T = 6, 4$ and 1.6 K ($< T_{N2}$) (red) and $T = 14, 12$ and 10 K ($> T_{N1}$) (blue). Their difference is drawn by the green line. Arrows denote the positions of magnetic Bragg peaks with the indicated wave vectors.

field ranges $35 < \mu_0 H < 46$ T and $34.9 < \mu_0 H < 44.6$ T calculated on the basis of the spin-1 Heisenberg TLAF and the classical Heisenberg-like TLAF with $|D|/J = 0.108$, respectively. Recent theory demonstrates that when a magnetic field is applied parallel to the symmetry axis, the field range of the quantum $1/3$ -magnetization plateau is enhanced by the easy-axis anisotropy and suppressed by the easy-plane anisotropy [16, 17]. Thus, it is suggested that the synergy between quantum fluctuation and the easy-axis anisotropy makes the field range of the $1/3$ -plateau wider for $H \parallel c$ in $\text{Ba}_2\text{La}_2\text{NiTe}_2\text{O}_{12}$. On the other hand, the easy-axis anisotropy will act to suppress the plateau width for $H \perp c$. Thus, it is considered that the plateau width depends on the angle between the magnetic field and the c axis, which leads to the distribution of the lower and higher edge fields H_{c1} and H_{c2} in a powdered sample. In addition, in case that the magnetic field is not exactly parallel to the c axis, the total spin is not conserved. Consequently, the $1/3$ -plateau does not become completely flat and has finite slope. These factors will give rise to the smearing of the $1/3$ -plateau in a powdered sample, as observed in the present measurement.

E. Magnetic structure

Next, we discuss the magnetic structure in the ordered phases in $\text{Ba}_2\text{La}_2\text{NiTe}_2\text{O}_{12}$. The neutron diffraction intensities averaged over $T = 14, 12, 10$ K ($> T_{N1} = 9.8$ K) and $T = 6, 4, 1.6$ K ($< T_{N2} = 8.9$ K) are shown in Fig. 11. There is a small but obvious difference between these ND intensities. Figure 12 shows powder ND spectra obtained at various temperatures, where the aver-

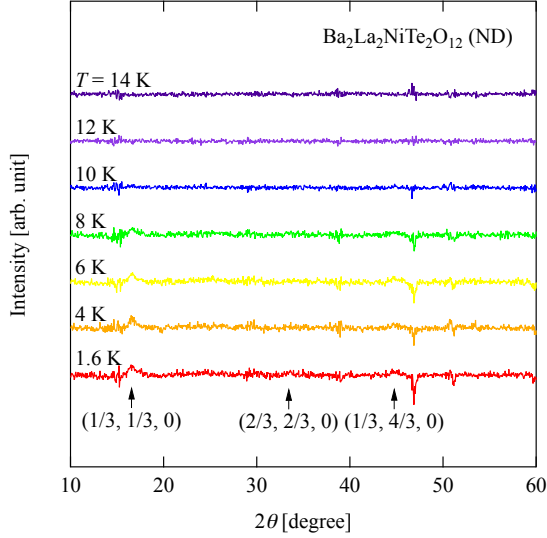


FIG. 12: (Color online) ND spectra collected at various temperatures, where the diffraction spectrum for $T > T_{N1}$ was subtracted as the background. Arrows indicate magnetic Bragg peaks with the indicated wave vectors. Lines for each temperature were arbitrarily shifted in the vertical direction.

age of the diffraction spectra obtained at $T = 14, 12, 10$ K was subtracted as the background. No magnetic peak is observed for $T \geq 10$ K. However, new peaks appear below 8 K, which is just below $T_{N2} = 8.9$ K. Thus, these new peaks can be attributed to magnetic Bragg peaks. Diffraction angles for some possible magnetic Bragg reflections, which are estimated from the lattice constants, are also indicated by arrows in Fig. 11. The diffraction angles calculated for $\mathbf{q} = (1/3, 1/3, 0)$ and its equivalent points coincide with the experimental results. This indicates that $\text{Ba}_2\text{La}_2\text{NiTe}_2\text{O}_{12}$ has a triangular spin structure characterized by the propagation vector $\mathbf{q} = (1/3, 1/3, 0)$ in the low temperature phase T_{N2} . This propagation vector is in contrast to $\mathbf{q} = (1/3, 1/3, 1/2)$ observed for $\text{Ba}_2\text{La}_2\text{CoTe}_2\text{O}_{12}$ [63]. The propagation vector $\mathbf{q} = (1/3, 1/3, 0)$ observed for $\text{Ba}_2\text{La}_2\text{NiTe}_2\text{O}_{12}$ implies that the Y-like triangular structures shown in Fig. 5(a) are ferromagnetically stacked along the c axis; thus, the weak resultant magnetic moments induced in the triangular layers are summed to produce a net moment along the c axis. This spin structure is consistent with the weak magnetic moment observed by magnetization measurement (see Figs. 4 and 6). In addition, we attempted to refine the size of the ordered magnetic moment of Ni^{2+} by the magnetic structure analysis of the ND data but failed owing to the weakness of the magnetic peaks.

F. Density functional theory calculations

The band structure of $\text{Ba}_2\text{La}_2\text{NiTe}_2\text{O}_{12}$ is shown in Fig. 13. There are five bands with dom-

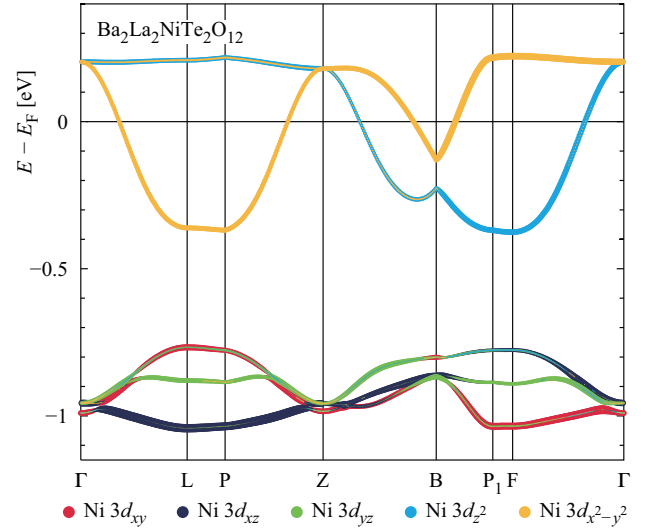


FIG. 13: (Color online) Band structure of $\text{Ba}_2\text{La}_2\text{NiTe}_2\text{O}_{12}$ obtained from GGA calculations. Orbital weights for Ni $3d$ orbitals are marked. The high-symmetry points for the rhombohedral space group are explained in the text.

inant Ni $3d$ character from the one Ni^{2+} ion in the unit cell. High-symmetry points in the Brillouin zone for the rhombohedral space group $R\bar{3}$ are named following Ref. [64]: $L = (1/2, 0, 0)$, $P = (\eta, \nu, \nu)$, $Z = (1/2, 1/2, 1/2)$, $B = (\eta, 1/2, 1 - \eta)$, $P_1 = (1 - \nu, 1 - \nu, 1 - \eta)$ and $F = (1/2, 1/2, 0)$, where $\eta = (1 + 4 \cos \alpha)/(2 + 4 \cos \alpha)$, $\nu = 3/4 - \eta/2$ and $\alpha = 33.889^\circ$ for $\text{Ba}_2\text{La}_2\text{NiTe}_2\text{O}_{12}$. Crossing the Fermi level, there are two bands of Ni e_g character, and below there are three bands of Ni t_{2g} character. The width of the two e_g bands is $W = 0.6$ eV, three times as large as the band width $W = 0.2$ eV in $\text{Ba}_2\text{La}_2\text{NiW}_2\text{O}_{12}$ (see Fig. 15 in the Appendix). As the hopping parameter, and thus the band width, enters the second-order perturbation estimate of the superexchange quadratically, we can expect the exchange couplings of $\text{Ba}_2\text{La}_2\text{NiTe}_2\text{O}_{12}$ to be almost an order of magnitude larger than those of $\text{Ba}_2\text{La}_2\text{NiW}_2\text{O}_{12}$.

We now proceed to determine the Heisenberg Hamiltonian parameters of $\text{Ba}_2\text{La}_2\text{NiTe}_2\text{O}_{12}$ using energy mapping. We fit all-electron DFT total energies to the Heisenberg Hamiltonian in the form

$$H = \sum_{i < j} J_{ij} \mathbf{S}_i \cdot \mathbf{S}_j. \quad (3)$$

We find that the total moments in all our calculations are exact multiples of $2\mu_B$ as all the nickel moments are exactly $S = 1$, and all the fits are very good, resulting in very low statistical errors. We first use a supercell with four Ni^{2+} ions to determine the two in-plane exchange couplings J_1 and J_3 , where we index the couplings with increasing Ni–Ni distance. The geometry of the Ni^{2+} ions in $\text{Ba}_2\text{La}_2\text{NiTe}_2\text{O}_{12}$ is shown as an inset in Fig. 14.

The values of the exchange constants are given in Ta-

TABLE III: Exchange couplings of $\text{Ba}_2\text{La}_2\text{NiTe}_2\text{O}_{12}$, calculated within GGA+U at $J_H = 0.88$ eV using a $6 \times 6 \times 6$ k mesh in a supercell containing four Ni^{2+} sites. The last row contains the Ni–Ni distances, which identify the exchange paths. The errors shown are only the statistical errors arising from the energy mapping.

U [eV]	J_1/k_B [K]	J_2/k_B [K]	J_3/k_B [K]	Θ_{CW} [K]
3	28.3(1)	-	0.09(1)	-113
3.5	25.2(1)	-	0.07(1)	-101
3.52	25.1(1)	-	0.07(1)	-100.7
4	22.6(1)	-	0.06(1)	-91
4.5	20.3(1)	-	0.05(1)	-81
5	18.2(1)	-	0.04(1)	-73
5.5	16.5(1)	-	0.03(1)	-66
6	14.9(1)	-	0.03(1)	-60
6.5	13.5(1)	-	0.02(1)	-54
7	12.2(1)	-	0.02(1)	-49
7.5	11.0(1)	-	0.02(1)	-44
8	10.0(1)	-	0.01(1)	-40
$d_{\text{Ni-Ni}}$ [Å]	5.66827	9.72442	9.81773	

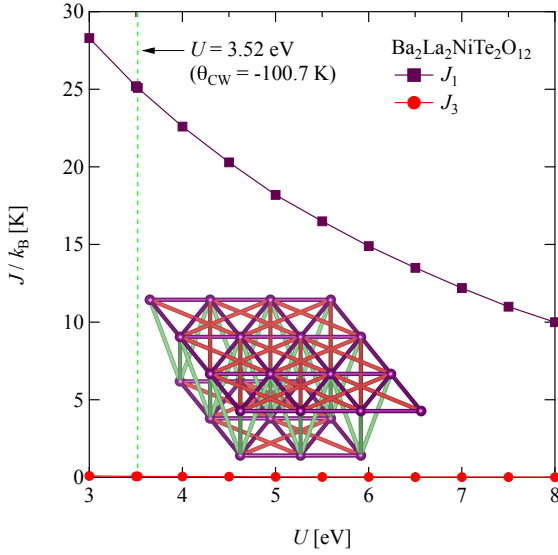


FIG. 14: (Color online) In-plane exchange couplings of $\text{Ba}_2\text{La}_2\text{NiTe}_2\text{O}_{12}$. The vertical line indicates the U value at which the experimental Curie–Weiss temperature is realized.

ble III. The values of J_i are given with respect to spin operators of length $S = 1$. Note that if the Hamiltonian is written as \sum_{ij} , counting every bond twice, then the values of J_i need to be divided by two. The Curie–Weiss temperatures are estimated from

$$\Theta_{\text{CW}} = -\frac{2}{3}S(S+1)(3J_1 + 3J_2 + 3J_3), \quad (4)$$

where $S = 1$.

The calculated exchange couplings are shown graphically in Fig. 14. The statistical errors are smaller than

TABLE IV: Exchange couplings of $\text{Ba}_2\text{La}_2\text{NiTe}_2\text{O}_{12}$, calculated within GGA+U at $J_H = 0.88$ eV with $4 \times 4 \times 4k$ points in a supercell containing six Ni^{2+} sites. The last row contains the Ni–Ni distances, which identify the exchange paths. The errors shown are only the statistical errors arising from the energy mapping.

U [eV]	J_1/k_B [K]	J_2/k_B [K]	J_3/k_B [K]	Θ_{CW} [K]
3	28.25(1)	0.024(1)	0.078(1)	-113
3.5	25.21(1)	0.022(1)	0.062(1)	-101
3.52	25.09(1)	0.021(1)	0.062(1)	-100.7
4	22.57(1)	0.018(1)	0.051(1)	-91
4.5	20.26(1)	0.016(1)	0.039(1)	-81
5	18.23(1)	0.014(1)	0.034(1)	-73
$d_{\text{Ni-Ni}}$ [Å]	5.66827	9.72442	9.81773	

the symbols. The inset shows the nickel sublattice of the defect perovskite $\text{Ba}_2\text{La}_2\text{NiTe}_2\text{O}_{12}$ with bonds indicating the first three exchange pathways. The nearest- and next-nearest-neighbor couplings of the triangular lattice are J_1 (purple) and J_3 (red), respectively. J_2 (turquoise) is the first-interlayer coupling. $U = 3.52$ eV was determined to be the value at which the couplings exactly yield the experimental Curie–Weiss temperature $\Theta_{\text{CW}} = -100.7$ K.

A larger supercell containing six inequivalent Ni^{2+} sites also allows the determination of the interlayer coupling J_2 . The result of this calculation is shown in Table IV. The interlayer coupling turns out to be even smaller than the next-nearest-neighbor coupling J_3 in the triangular lattice. However, consistent with the fact that the calculation with the four- Ni^{2+} unit cell does not allow the separation of J_1 and J_2 , meaning that the J_1 values in Table III actually represent the sum $J_1 + J_2$, the new J_1 values in Table IV are very slightly smaller than those in Table III. However, this more precise calculation still has not yielded a substantial subleading coupling to the antiferromagnetic J_1 . The U value that can reproduce the experimental Curie–Weiss temperature $\Theta_{\text{CW}} = -100.7$ K is still $U = 3.52$ eV.

From these DFT calculations, $\text{Ba}_2\text{La}_2\text{NiTe}_2\text{O}_{12}$ was found to be a pure triangular lattice antiferromagnet with a nearly negligible next-neighbor coupling in the plane. However, as the interlayer Ni–Ni distance is comparable to the in-plane next-neighbor distance, we also determined this additional coupling using larger supercells for the energy mapping. However, these calculations indicate that $\text{Ba}_2\text{La}_2\text{NiTe}_2\text{O}_{12}$ is, as a very good approximation, a 2D triangular lattice antiferromagnet. The only interlayer coupling we were able to resolve, J_2 , is tiny and antiferromagnetic. Thus, the small ferromagnetic coupling between the layers that was experimentally inferred from the weak magnetic moment at zero field could, for example, arise from the as yet unknown J_4 at a distance of $d_{\text{Ni-Ni}} = 11.256$ Å.

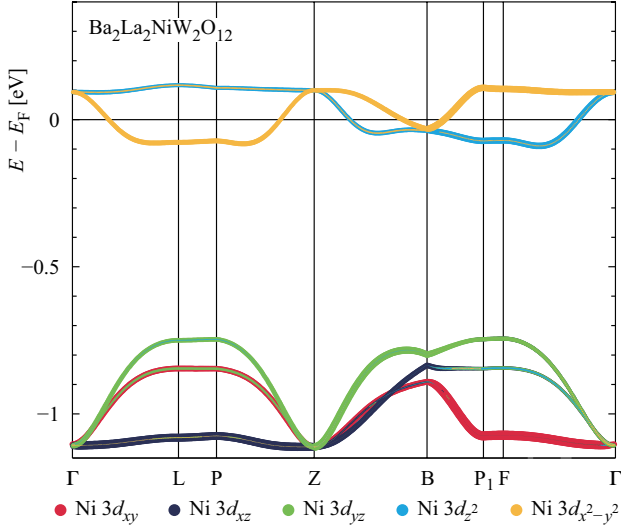


FIG. 15: (Color online) Band structure of $\text{Ba}_2\text{La}_2\text{NiW}_2\text{O}_{12}$ obtained from GGA calculations. Orbital weights for Ni $3d$ orbitals are marked.

V. CONCLUSION

We have reported on the crystal structure and magnetic properties of the spin-1 TLAF $\text{Ba}_2\text{La}_2\text{NiTe}_2\text{O}_{12}$ composed of a uniform triangular lattice of Ni^{2+} ions. We refined the crystal structure parameters by Rietveld analysis using XRD and ND data obtained from a powdered sample. The space group was determined to be $R\bar{3}$. The large negative Weiss constant $\Theta_{\text{CW}} \simeq -100$ K for the magnetic susceptibility shows that the predominant exchange interaction is antiferromagnetic and strong, in contrast to $\text{Ba}_2\text{La}_2\text{NiW}_2\text{O}_{12}$ [43, 44]. Specific heat measurement demonstrated that $\text{Ba}_2\text{La}_2\text{NiTe}_2\text{O}_{12}$ undergoes successive magnetic phase transitions at $T_{\text{N1}} = 9.8$ K and at $T_{\text{N2}} = 8.9$ K, which arise from the competition between the antiferromagnetic exchange interaction and the single-ion anisotropy of the easy-axis type. From the weak net magnetic moment of $\bar{\Delta M} = 0.015 \mu_{\text{B}}/\text{Ni}^{2+}$ observed at $T = 1.8$ K ($\ll T_{\text{N2}}$), the ratio of single-ion anisotropy to the exchange interaction was estimated as $|D|/J \simeq 0.108$. It was found from high-magnetic-field magnetization measurement up to 60 T that the mag-

netization curve exhibits a wide plateau at one-third of the saturation magnetization, which is characteristic of 2D Heisenberg-like TLAFs. We estimated the exchange interaction J and the g -factor as $J/k_{\text{B}} \simeq 19$ K and $g \simeq 2.3$, respectively, by fitting the theoretical magnetization curve to the experimental data. From the ND measurements at zero magnetic field, the propagation vector in the low-temperature phase for $T < T_{\text{N2}}$ was found to be $\mathbf{q} = (1/3, 1/3, 0)$. This result, together with the magnetization and specific heat results, indicates that below T_{N2} , spins form a triangular structure in a plane including the c axis in each triangular layer and these triangular spin structures are ferromagnetically stacked along the c axis. The DFT calculations demonstrated that the nearest-neighbor exchange interaction is predominant and that the next-nearest-neighbor exchange interaction in the triangular layer and the interlayer exchange interactions are negligible.

Acknowledgments

We thank the authors of Ref. [14] for allowing us to use their theoretical calculations of the magnetization process. This work was supported by Grants-in-Aid for Scientific Research (A) (No. 17H01142) and (C) (No. 16K05414) from Japan Society for the Promotion of Science.

Appendix A: Electronic structure of $\text{Ba}_2\text{La}_2\text{NiW}_2\text{O}_{12}$

For comparison with the new material $\text{Ba}_2\text{La}_2\text{NiTe}_2\text{O}_{12}$, we have determined the electronic structure of $\text{Ba}_2\text{La}_2\text{NiW}_2\text{O}_{12}$ using the crystal structure provided in Ref. [43]. Figure 15 shows the bands calculated with the GGA exchange correlation functional. The path through the Brillouin zone is explained in the main text. As in isostructural $\text{Ba}_2\text{La}_2\text{NiTe}_2\text{O}_{12}$, two Ni $3d$ bands of e_g character cross the Fermi level. However, the band width is only 0.2 eV, indicating rather small effective hopping parameters between Ni e_g orbitals compared to $\text{Ba}_2\text{La}_2\text{NiTe}_2\text{O}_{12}$.

- [1] M. F. Collins and O. A. Petrenko, Triangular antiferromagnets, *Can. J. Phys.* **75**, 605 (1997).
- [2] O. A. Starykh, Unusual ordered phases of highly frustrated magnets: a review, *Rep. Prog. Phys.* **78**, 052502 (2015).
- [3] S. Miyashita, Magnetic properties of Ising-like Heisenberg antiferromagnets on the triangular lattice, *J. Phys. Soc. Jpn.* **55**, 3605 (1986).
- [4] H. Kitazawa, H. Suzuki, H. Abe, J. Tang, and G. Kido, High-field magnetization of triangular lattice antiferro-

- magnet: GdPd_2Al_3 , *Physica B* **259-261**, 890 (1999).
- [5] T. Inami, N. Terada, H. Kitazawa, and O. Sakai, Resonant magnetic X-ray diffraction study on the triangular lattice antiferromagnet GdPd_2Al_3 , *J. Phys. Soc. Jpn.* **78**, 084713 (2009).
- [6] R. Ishii, S. Tanaka, K. Onuma, Y. Nambu, M. Tokunaga, T. Sakakibara, N. Kawashima, Y. Maeno, C. Broholm, D. P. Gautreaux, J. Y. Chan, and S. Nakatsuji, Successive phase transitions and phase diagrams for the quasi-two-dimensional easy-axis triangular antiferromag-

- net $\text{Rb}_4\text{Mn}(\text{MoO}_4)_3$, *Europhys. Lett.* **94**, 17001 (2011).
- [7] H. Nishimori and S. Miyashita, Magnetization process of the spin-1/2 antiferromagnetic Ising-like Heisenberg model on the triangular lattice, *J. Phys. Soc. Jpn.* **55**, 4448 (1986).
- [8] A. V. Chubokov and D. I. Golosov, Quantum theory of an antiferromagnet on a triangular lattice in a magnetic field, *J. Phys.: Condens. Matter* **3**, 69 (1991).
- [9] T. Nikuni and H. Shiba, Quantum fluctuations and magnetic structures of CsCuCl_3 in high magnetic fields, *J. Phys. Soc. Jpn.* **62**, 3268 (1993).
- [10] A. Honecker, A comparative study of the magnetization process of two-dimensional antiferromagnets, *J. Phys.: Condens. Matter* **11**, 4697 (1999).
- [11] J. Alicea, A. V. Chubokov, and O. A. Starykh, Quantum stabilization of the 1/3-magnetization plateau in Cs_2CuBr_4 , *Phys. Rev. Lett.* **102**, 137201 (2009).
- [12] D. J. J. Farnell, R. Zinke, J. Schulenburg, and J. Richter, High-order coupled cluster method study of frustrated and unfrustrated quantum magnets in external magnetic fields, *J. Phys.: Condens. Matter* **21**, 406002 (2009).
- [13] T. Sakai and H. Nakano, Critical magnetization behavior of the triangular- and kagome-lattice quantum antiferromagnets, *Phys. Rev. B* **83**, 100405(R) (2011).
- [14] J. Richter, O. Götze, R. Zinke, D. J. J. Farnell, and H. Tanaka, The magnetization process of the spin-one triangular-lattice Heisenberg antiferromagnet, *J. Phys. Soc. Jpn.* **82**, 015002 (2013).
- [15] C. Hotta, S. Nishimoto, and N. Shibata, Grand canonical finite size numerical approaches in one and two dimensions: real space energy renormalization and edge state generation, *Phys. Rev. B* **87**, 115128 (2013).
- [16] D. Yamamoto, G. Marmorini, and I. Danshita, Quantum phase diagram of the triangular-lattice XXZ model in a magnetic field, *Phys. Rev. Lett.* **112**, 127203 (2014).
- [17] D. Sellmann, X. F. Zhang, and S. Eggert, Phase diagram of the antiferromagnetic XXZ model on the triangular lattice, *Phys. Rev. B* **91**, 081104(R) (2015).
- [18] T. Coletta, T. A. Tóth, K. Penc, and F. Mila, Semiclassical theory of the magnetization process of the triangular lattice Heisenberg model, *Phys. Rev. B* **94**, 075136 (2016).
- [19] T. Ono, H. Tanaka, H. Aruga Katori, F. Ishikawa, H. Mitamura, and T. Goto, Magnetization plateau in the frustrated quantum spin system Cs_2CuBr_4 , *Phys. Rev. B* **67**, 104431 (2003).
- [20] T. Ono, H. Tanaka, O. Kolomiets, H. Mitamura, T. Goto, K. Nakajima, A. Oosawa, Y. Koike, K. Kakurai, J. Klenke, P. Smeibidle, and M. Meißner, Magnetization plateaux of the $S = 1/2$ two-dimensional frustrated antiferromagnet Cs_2CuBr_4 , *J. Phys.: Condens. Matter* **16**, S773 (2004).
- [21] N. A. Fortune, S. T. Hannahs, Y. Yoshida, T. E. Sherrington, T. Ono, H. Tanaka, and Y. Takano, Cascade of magnetic-field-induced quantum phase transitions in a spin- $\frac{1}{2}$ triangular-lattice antiferromagnet, *Phys. Rev. Lett.* **102**, 257201 (2009).
- [22] Y. Shirata, H. Tanaka, A. Matsuo, and K. Kindo, Experimental Realization of a Spin-1/2 Triangular-Lattice Heisenberg Antiferromagnet, *Phys. Rev. Lett.* **108**, 057205 (2012).
- [23] H. D. Zhou, C. Xu, A. M. Hallas, H. J. Silverstein, C. R. Wiebe, I. Umegaki, J. Q. Yan, T. P. Murphy, J.-H. Park, Y. Qiu, J. R. D. Copley, J. S. Gardner, and Y. Takano, Successive phase transitions and extended spin-excitation continuum in the $S = 1/2$ triangular-lattice antiferromagnet $\text{Ba}_3\text{CoSb}_2\text{O}_9$, *Phys. Rev. Lett.* **109**, 267206 (2012).
- [24] T. Susuki, N. Kurita, T. Tanaka, H. Nojiri, A. Matsuo, K. Kindo, and H. Tanaka, Magnetization process and collective excitations in the $S = 1/2$ triangular-lattice Heisenberg antiferromagnet $\text{Ba}_3\text{CoSb}_2\text{O}_9$, *Phys. Rev. Lett.* **110**, 267201 (2013).
- [25] G. Quirion, M. Lapointe-Major, M. Poirier, J. A. Quilliam, Z. L. Dun, and H. D. Zhou, Magnetic phase diagram of $\text{Ba}_3\text{CoSb}_2\text{O}_9$ as determined by ultrasound velocity measurements, *Phys. Rev. B* **92**, 014414 (2015).
- [26] G. Koutroulakis, T. Zhou, Y. Kamiya, J. D. Thompson, H. D. Zhou, C. D. Batista, and S. E. Brown, Quantum phase diagram of the $S = \frac{1}{2}$ triangular-lattice antiferromagnet $\text{Ba}_3\text{CoSb}_2\text{O}_9$, *Phys. Rev. B* **91**, 024410 (2015).
- [27] A. Sera, Y. Kousaka, J. Akimitsu, M. Sera, and K. Inoue, Pressure-induced quantum phase transitions in the $S = \frac{1}{2}$ triangular lattice antiferromagnet CsCuCl_3 , *Phys. Rev. B* **96**, 014419 (2017).
- [28] O. A. Starykh, W. Jin, and A. V. Chubokov, Phases of a triangular-lattice antiferromagnet near saturation, *Phys. Rev. Lett.* **113**, 087204 (2014).
- [29] D. Yamamoto, G. Marmorini, and I. Danshita, Microscopic model calculations for the magnetization process of layered triangular-lattice quantum antiferromagnets, *Phys. Rev. Lett.* **114**, 027201 (2015).
- [30] J. Ma, Y. Kamiya, T. Hong, H. B. Cao, G. Ehlers, W. Tian, C. D. Batista, Z. L. Dun, H. D. Zhou, and M. Matsuda, Static and dynamical properties of the spin-1/2 equilateral triangular-lattice antiferromagnet $\text{Ba}_3\text{CoSb}_2\text{O}_9$, *Phys. Rev. Lett.* **116**, 087201 (2016).
- [31] S. Ito, N. Kurita, H. Tanaka, S. Ohira-Kawamura, K. Nakajima, S. Itoh, K. Kuwahara, and K. Kakurai, Structure of the magnetic excitations in the spin-1/2 triangular-lattice Heisenberg antiferromagnet $\text{Ba}_3\text{CoSb}_2\text{O}_9$, *Nat. Commun.* **8**, 235 (2017).
- [32] Y. Kamiya, L. Ge, Tao Hong, Y. Qiu, D. L. Quintero-Castro, Z. Lu, H. B. Cao, M. Matsuda, E. S. Choi, C. D. Batista, M. Mourigal, H. D. Zhou, and J. Ma, The nature of spin excitations in the one-third magnetization plateau phase of $\text{Ba}_3\text{CoSb}_2\text{O}_9$, *Nat. Commun.* **9**, 2666 (2018).
- [33] O. A. Starykh, A. V. Chubokov, and A. G. Abanov, Flat spin-wave dispersion in a triangular antiferromagnet, *Phys. Rev. B* **74**, 180403(R) (2006).
- [34] W. H. Zheng, J. O. Fjærestad, R. R. P. Singh, R. H. McKenzie, and R. Coldea, Excitation spectra of the spin- $\frac{1}{2}$ triangular-lattice Heisenberg antiferromagnet, *Phys. Rev. B* **74**, 224420 (2006).
- [35] A. L. Chernyshev and M. E. Zhitomirsky, Spin waves in a triangular lattice antiferromagnet: decays, spectrum renormalization, and singularities, *Phys. Rev. B* **79**, 144416 (2009).
- [36] A. Mezio, C. N. Sposetti, L. O. Manuel, and A. E. Trumper, A test of the bosonic spinon theory for the triangular antiferromagnet spectrum, *Europhys. Lett.* **94**, 47001 (2011).
- [37] M. Mourigal, W. T. Fuhrman, A. L. Chernyshev, and M. E. Zhitomirsky, Dynamical structure factor of the triangular-lattice antiferromagnet, *Phys. Rev. B* **88**, 094407 (2013).
- [38] E. A. Ghioldi, A. Mezio, L. O. Manuel, R. R. R. Singh,

- J. Oitmaa, and A. E. Trumper, Magnons and excitation continuum in XXZ triangular antiferromagnetic model: application to $\text{Ba}_3\text{CoSb}_2\text{O}_9$, *Phys. Rev. B* **91**, 134423 (2015).
- [39] E. A. Ghioldi, M. G. Gonzalez, S.-S. Zhang, Y. Kamiya, L. O. Manuel, A. E. Trumper, and C. D. Batista, Dynamical structure factor of the triangular antiferromagnet: Schwinger boson theory beyond mean field, *Phys. Rev. B* **98**, 184403 (2018).
- [40] H.-D. Autenrieth and S. Kemmler-Sack, Kathodo- und Photolumineszenz der Seltenerd-aktivierten Wirtsgitter $\text{Ba}_2\text{La}_2\text{B}^{2+}\text{Te}_2\text{O}_{12}$ ($\text{B} = \text{Zn, Mg}$), *Z. Naturforsch. A* **41**, 866 (1986).
- [41] S. Kemmler-Sack, Die rhomboedrischen 12 L-Stapelvarianten $\text{Ba}_2\text{La}_2\text{B}^{\text{II}}(\text{W}_2^{\text{VI}}\square\text{O}_{12})$, *Z. Anorg. Allg. Chem.* **461**, 142 (1980).
- [42] Z. Li, J. Sun, L. You, Y. Wang, and J. Lin, Synthesis and crystal structure of $\text{Ba}_2\text{La}_2\text{MnW}_2\text{O}_{12}$, *J. Alloys Compd.* **379**, 117 (2004).
- [43] R. Rawl, M. Lee, E. S. Choi, G. Li, K. W. Chen, R. Baumbach, C. R. Dela Cruz, J. Ma, and H. D. Zhou, Magnetic properties of the triangular lattice magnets $A_4B'B_2\text{O}_{12}$ ($A=\text{Ba, Sr, La}$; $B'=\text{Co, Ni, Mn}$; $B=\text{W, Re}$), *Phys. Rev. B* **95**, 174438 (2017).
- [44] Y. Doi, M. Wakeshima, K. Tezuka, Y. J. Shan, K. Ohoyama, S. Lee, S. Torii, T. Kamiyama, and Y. Hinatsu, Crystal structures, magnetic properties, and DFT calculation of B-site defected 12L-perovskites $\text{Ba}_2\text{La}_2\text{MW}_2\text{O}_{12}$ ($M = \text{Mn, Co, Ni, Zn}$), *J. Phys.: Condens. Matter* **29**, 365802 (2017).
- [45] K. Yokota, N. Kurita, and H. Tanaka, Magnetic phase diagram of the $S = 1/2$ triangular-lattice Heisenberg antiferromagnet $\text{Ba}_3\text{CoNb}_2\text{O}_9$, *Phys. Rev. B* **90**, 014403 (2014).
- [46] T. Koga, N. Kurita, M. Avdeev, S. Danilkin, T. J. Sato, and H. Tanaka, Magnetic structure of the $S = \frac{1}{2}$ quasi-two-dimensional square-lattice Heisenberg antiferromagnet $\text{Sr}_2\text{CuTeO}_6$, *Phys. Rev. B* **93**, 054426 (2016).
- [47] F. Izumi and K. Momma, Three-dimensional visualization in powder diffraction, *Solid State Phenom.* **130**, 15 (2007).
- [48] K. Koepernik and H. Eschrig, Full-potential nonorthogonal local-orbital minimum-basis band-structure scheme, *Phys. Rev. B* **59**, 1743 (1999).
- [49] J. P. Perdew, K. Burke, and M. Ernzerhof, Generalized gradient approximation made simple, *Phys. Rev. Lett.* **77**, 3865 (1996).
- [50] D. Guterding, R. Valentí, and H. O. Jeschke, Reduction of magnetic interlayer coupling in barlowite through isoelectronic substitution, *Phys. Rev. B* **94**, 125136 (2016).
- [51] Y. Iqbal, T. Müller, K. Riedl, J. Reuther, S. Rachel, R. Valentí, M. J. P. Gingras, R. Thomale, and H. O. Jeschke, Signatures of a gearwheel quantum spin liquid in a spin-1/2 pyrochlore molybdate Heisenberg antiferromagnet, *Phys. Rev. Mater.* **1**, 071201(R) (2017).
- [52] Y. Iqbal, T. Müller, H. O. Jeschke, R. Thomale, and J. Reuther, Stability of the spiral spin liquid in MnSc_2S_4 , *Phys. Rev. B* **98**, 064427 (2018).
- [53] A. I. Liechtenstein, V. I. Anisimov, and J. Zaanen, Density-functional theory and strong interactions: orbital ordering in Mott-Hubbard insulators, *Phys. Rev. B* **52**, R5467(R) (1995).
- [54] T. Mizokawa and A. Fujimori, Electronic structure and orbital ordering in perovskite-type 3d transition-metal oxides studied by Hartree-Fock band-structure calculations, *Phys. Rev. B* **54**, 5368 (1996).
- [55] J. Tapp, C. R. dela Cruz, M. Bratsch, N. E. Amuneke, L. Postulka, B. Wolf, M. Lang, H. O. Jeschke, R. Valentí, P. Lemmens, and A. Möller, From magnetic order to spin-liquid ground states on the $S = 3/2$ triangular lattice, *Phys. Rev. B* **96**, 064404 (2017).
- [56] Y. Doi, Y. Hinatsu, and K. Ohoyama, Structural and magnetic properties of pseudo-two-dimensional triangular antiferromagnets $\text{Ba}_3\text{MSb}_2\text{O}_9$ ($M=\text{Mn, Co, and Ni}$), *J. Phys.: Condens. Matter* **16**, 8923 (2004).
- [57] Y. Shirata, H. Tanaka, T. Ono, A. Matsuo, K. Kindo, and H. Nakano, Quantum magnetization plateau in spin-1 triangular-lattice antiferromagnet $\text{Ba}_3\text{NiSb}_2\text{O}_9$, *J. Phys. Soc. Jpn.* **80**, 093702 (2011).
- [58] F. Matsubara, Magnetic ordering in a hexagonal antiferromagnet, *J. Phys. Soc. Jpn.* **51**, 2424 (1982).
- [59] K. Watanabe, H. Kawamura, H. Nakano, and T. Sakai, Quantum spin-liquid behavior in the spin-1/2 random Heisenberg antiferromagnet on the triangular lattice, *J. Phys. Soc. Jpn.* **83**, 034714 (2014).
- [60] H. Kawamura, K. Watanabe, and T. Shimokawa, Quantum spin-liquid behavior in the spin-1/2 random-bond Heisenberg antiferromagnet on the kagome lattice, *J. Phys. Soc. Jpn.* **83**, 103704 (2014).
- [61] H. Kawamura and S. Miyashita, Phase transition of the Heisenberg antiferromagnet on the triangular lattice in a magnetic field, *J. Phys. Soc. Jpn.* **54**, 4530 (1985).
- [62] L. Seabra, T. Momoi, P. Sindzingre, and N. Shannon, Phase diagram of the classical Heisenberg antiferromagnet on a triangular lattice in an applied magnetic field, *Phys. Rev. B* **84**, 214418 (2011).
- [63] Y. Kojima, M. Watanabe, N. Kurita, H. Tanaka, A. Matsuo, K. Kindo, and M. Avdeev, Quantum magnetic properties of the spin- $\frac{1}{2}$ triangular-lattice antiferromagnet $\text{Ba}_2\text{La}_2\text{CoTe}_2\text{O}_{12}$, *Phys. Rev. B* **98**, 174406 (2018).
- [64] W. Setyawan and S. Curtarolo, High-throughput electronic band structure calculations: challenges and tools, *Comput. Mater. Sci.* **49**, 299 (2010).